


 Cite this: *CrystEngComm*, 2020, 22, 2933

Flexible bifunctional monoethylphosphonate/ carboxylates of Zn(II) and Co(II) reinforced with DABCO co-ligand: paradigmatic structural organization with pcu topology†

 Anna Goldman,^a Beatriz Gil-Hernández,^b Simon Millan,^a Serkan Gökpinar,^a Christian Heering,^a Ishtvan Boldog^{id}*^a and Christoph Janiak^{id}*^a

Two novel isostructural phosphonate-monoethylcarboxylate MOFs with the structural formula of $[M_2(\text{EtBCP})_2(\text{DABCO})_{0.5}] \cdot 2\text{DMA}$ ($M = \text{Zn}$ (**2**), Co (**3**); $\text{H}_2\text{EtBCP} = O$ -ethyl- P -(4-carboxyphenyl)phosphonic acid, $\text{DABCO} = 1,4$ -diazabicyclo[2.2.2]octane, $\text{DMA} = N,N$ -dimethylacetamide) were synthesized and characterized. The frameworks of **2** and **3** are sustained by $\{\text{Zn}_2(\text{PO}_2(\text{OEt})_2)_n\}$ metal-phosphonate- and DABCO-extended $\{\text{Zn}_2(\text{COO})_4(\text{DABCO})\}_n$ paddle-wheel carboxylate chain-SBUs. The chains providing connectivity in three, mutually orthogonal directions are running parallel and are combined in a framework, which could be interpreted as having a **pcu** topology. The simple structure-organization principle, which suggests the possibility of the elongation of the bifunctional ligand with scaling in two directions, allows to view the structures of **2** and **3** as prototypes for an isorecticular series. The porosity of both compounds, based on a relatively short ligand, is low: no adsorption of N_2 was registered, however, CO_2 is adsorbed readily allowing to estimate the surface area at $\sim 330 \text{ m}^2 \text{ g}^{-1}$ (~ 900 – $1060 \text{ m}^2 \text{ g}^{-1}$ geometric estimate). The compounds demonstrate a two-step CO_2 adsorption isotherm both at 195 K (0–1 bar) and 298 K (0–20 bar). The adsorption isotherms are characterized by a gradual (type “F-I”), albeit still relatively steep onset of the second step, associated with structural flexibility/bistability. The estimated pore volumes at the start of the transformation (195 K) for **2** and **3** are ~ 0.11 ($0.08P/P_0$) and $0.12 \text{ cm}^3 \text{ g}^{-1}$ ($0.12P/P_0$) respectively, which corresponds considerably well to the geometrically calculated accessible volume of $\sim 0.07 \text{ cm}^3 \text{ g}^{-1}$ for the experimental structure (3.3 Å probe diameter). The structural prerequisites of the observed flexibility of the framework, which might be associated with the non-planarity of the metal-phosphonate moieties, acting as ‘levers’ for propagating mechanical stress, are discussed.

 Received 25th February 2020,
Accepted 31st March 2020

DOI: 10.1039/d0ce00275e

rsc.li/crystengcomm

Introduction

The field of metal-organic frameworks (MOFs) witnessed explosive growth during the last two decades. The ‘hybrid’ nature of the coordination polymers, consisting of both inorganic and organic constituents, their crystallinity and high attainable surface areas are among the primary factors behind the great expectations.

The structural versatility and functional tunability^{1–3} of MOF materials are indeed superior and a range of possible applications are demonstrated, including gas storage, small molecule separation, catalysis, sensing *etc.*^{4–7} On the other hand, the relatively low chemical/hydrolytic stability is a hindrance to their real-world use. Nearly all of the most stable MOFs are $M(\text{III}, \text{IV}) = \text{Cr}, \text{Fe}, \text{Al}, \text{Zr}$ carboxylates and $M(\text{I}, \text{II}) = \text{Ag}, \text{Cu}, \text{Zn}, \text{Co}$ azolates. The bidentate phosphinates⁸ and particularly the tridentate phosphonates of oxophilic⁹ metals possess the thermodynamic prerequisites to be more stable than carboxylates (even if the kinetic factors could often prevail). Porous organo-phosphonates are actively researched for more than a decade, however the achievements were modest until recently. There is a strong tendency towards formation of dense layered structures,¹⁰ partly evident for linear arylphosphonates (the stacking of the aryl-moiety reinforces the dense parallel packing; the use

^a Institut für Anorganische Chemie und Strukturchemie, Heinrich-Heine-Universität Düsseldorf, D-40204 Düsseldorf, Germany. E-mail: janiak@hhu.de

^b Departamento de Química, Facultad de Ciencias de La Laguna, Sección Química, Universidad de La Laguna, 38206 La Laguna, Tenerife, Spain

† Electronic supplementary information (ESI) available: Experimental details and characterization data. CCDC 1985570 and 1985571. For ESI and crystallographic data in CIF or other electronic format see DOI: 10.1039/d0ce00275e

of non-acrylic ligand platforms, namely (bi)piperidines, led to one of the most successful early phosphonate MOFs, the isoreticular STA-12, -16 (ref. 11 and 12)). Discrete secondary building units (SBUs) tend to be less frequent compared to infinite 1D or 2D cases, which favor dense packing, due to relatively high denticity of the phosphonate group.¹³

The analysis of the relatively rare phosphonates with high porosity suggests a few strategies to avoid dense structures. The use of large rigid molecules with non-collinear phosphonate branches, *e.g.* trigonal shaped¹⁴ or even better non-coplanar, *e.g.* tetragonal shaped molecules,¹⁵ is one of the approaches.^{16,17} The recent report of the ultrastable highly porous zirconium-based SZ series (S_{BET} up to $\sim 600 \text{ m}^2 \text{ g}^{-1}$ for $[\text{N-Et-pyridinium}]_2[\text{Zr}_{3.5}(\text{LH})\text{F}_9]$)¹⁵ with nearly fully deprotonated tetrahedral adamantane tetraphosphonic acids (H_8L) crowned the efforts of this type and the use of ionic liquids as a medium suggests the possibility of templating. The microporous CAU-14 copper phosphonate¹⁴ with modest CO_2 adsorption is also worth mentioning.

Alternatively, the introduction of synergistic co-ligands, *e.g.* N-donor ligands, or the use of monoalkylphosphonates for the decrease of the ligand's denticity were proven also efficient.

The use of N-donor co-ligands was shown to be partially productive leading to 3D framework compounds incorporating 2,2'-bipyridine, 1,10-phenanthroline, 4,4'-bipyridine or 4,4'-trimethylenedipyridine.^{18–21} For most of the compounds no permanent porosities were demonstrated, however, extensive reports on properties including luminescence,^{22–25} magnetism,^{26–28} catalysis,²⁹ thermal stability^{30,31} and water stability^{32,33} were published. It is important to note, that the combination of carboxylate and N-donor ligands for divalent 3d metals is a viable strategy for the increase of stability. An illustrative example are the $[\text{M}(\text{BDC})_2(\text{DABCO})]$, $\text{M} = \text{Cu}, \text{Zn}$ MOFs, which demonstrate significantly higher hydrolytic stability than the carboxylate-only peers.^{34,35} The role of the N-donor ligands could also be interpreted as a means of decreasing the average local connectivity of the networks. Other, more synergistic cases could be also foreseen. Monoesters of phosphonic acids and phosphinates are both bidentate and could function analogously to carboxylate groups.³⁶ The seminal works of Shimizu *et al.*,^{36–38} eventually lead to the discovery of the permanently porous copper monoesterphosphonate framework CALF-33- Et_3 (CALF = Calgary Framework) with one of the highest surface areas at $1000 \text{ m}^2 \text{ g}^{-1}$ for a phosphonate-based MOF.^{31,39} It is expected, that the alkyl substituent could tune the adsorption preference of the smaller CO_2 molecules over N_2 and CH_4 .^{40,41}

The use of phosphonate-monoesters as ligands for the synthesis of MOFs with significant porosity is also known; the reported materials are often characterized by high moisture and water-vapor stability.^{42–44} Selected examples of the respective monoesterphosphonic acids used for the syntheses of coordination polymers/MOFs are summarized in Fig. 1.

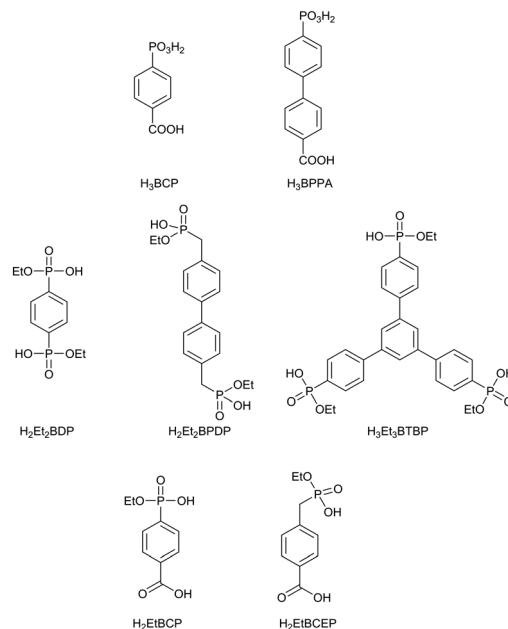


Fig. 1 The most relevant phosphonic and monoesterphosphonic acids reported in the literature as building-blocks for MOFs.^{21,32,36,39,41}

Our research was inspired by all the three mentioned strategies aiming for robust phosphonate MOFs: the use of bifunctional (monoalkyl)phosphonates, their potentially synergistic combination with carboxylate functions in one ligand, and the use of N-donor co-ligands. Herein, we report two novel isostructural monoethylphosphonate-carboxylate MOFs obtained using that strategy: $[\text{Zn}_2(\text{EtBCP})_2(\text{DABCO})_{0.5}] \cdot 2\text{DMA}$, **2** and $[\text{Co}_2(\text{EtBCP})_2(\text{DABCO})_{0.5}] \cdot 2\text{DMA}$, **3**, with $\text{H}_2\text{EtBCP} = \text{O-ethyl-}P\text{-}(4\text{-carboxyphenyl})\text{phosphonic acid}$, the second only known ligand of this class used for the syntheses of coordination polymers. The implications, originating from the potentially general importance of their special structures and the structural flexibility observed from the CO_2 adsorption data are discussed.

Results and discussion

Synthesis and structural characterization

The ligand, *O*-ethyl-*P*-(4-carboxyphenyl)phosphonic acid (H_2EtBCP), was synthesized in two steps. The intermediary diethyl *P*-(4-carboxyphenyl)phosphonate was obtained by the Ni(II)-catalyzed Michaelis–Arbuzov reaction between the methyl 4-iodobenzoate with triethylphosphite. Partial hydrolysis in 2 mol L^{-1} aqueous NaOH under mild conditions yielded the aimed monoester, H_2EtBCP (see the experimental section for details). While H_2EtBCP was reported before,^{45–47} it was never used for the synthesis of coordination polymers. It is a rigid ligand, which is the second only representative of the monoalkylphosphonic-carboxylic acid class used in the synthesis of coordination polymers/MOFs after the flexible *O*-ethyl-*P*-(4-carboxyphenylmethyl)phosphonic acid (H_2EtBCEP) used for the preparation of non-porous luminescent

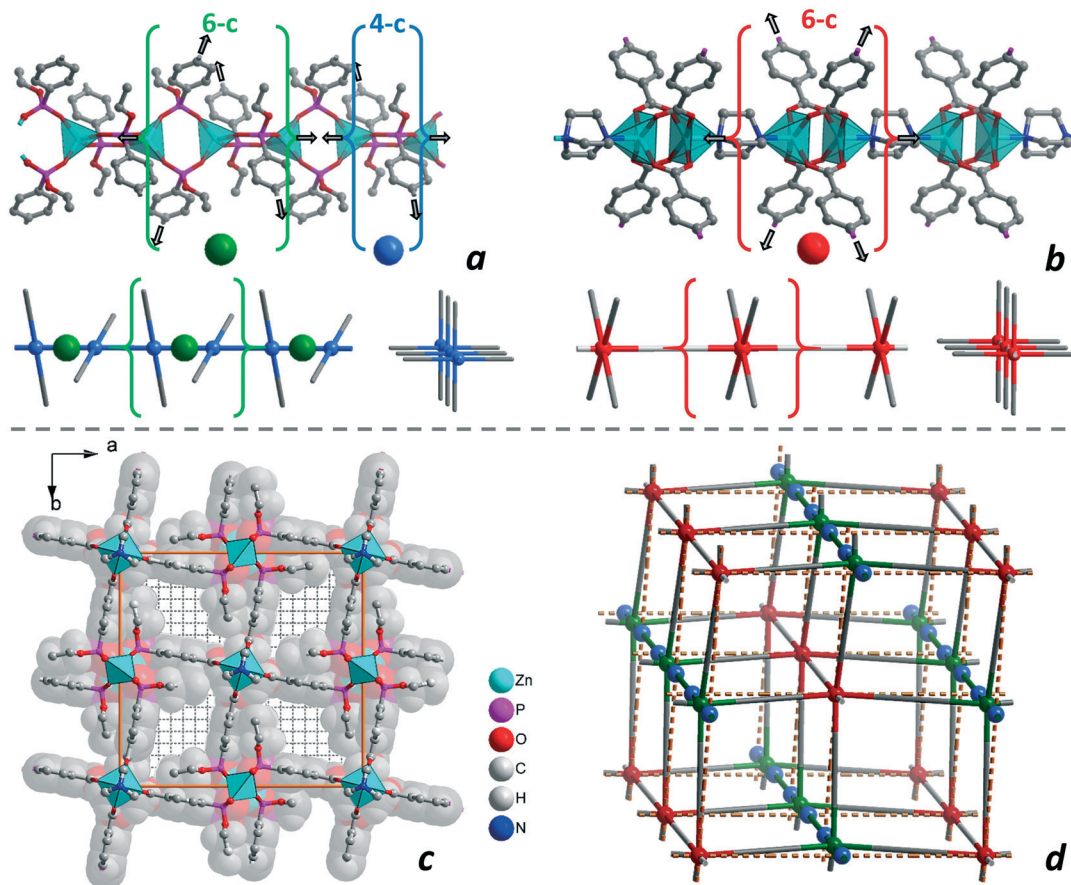


Fig. 5 The structural organization of **2** and **3**: (a) the $\{Zn_2(PO_2(OEt)_2)_2\}_n$ phosphonate-monoester chain-SBU; the 4-c $\{Zn_2(PO_2(OEt)_2)_2\}$ and the 6-c $\{Zn_2(PO_2(OEt)_2)_2\}$ topological node interpretations are explained under the molecular drawing. (b) The $\{Zn_2(COO)_4(DABCO)\}_n$ extended paddle-wheel chain-SBU sustained by standard paddle-wheel units, joined axially by the bridging DABCO molecules. (c) The view on the framework along the c-axis (no H-atoms are shown for clarity) with an underlay-image of the ball-and-stick model image (with H-atoms shown) and a 1 Å grid, limited to the pores. (d) A topological representation of the framework, with the primary interpretation as a 6,6-c net (green and red nodes, **pcu**). The alternative connections on the level of the 4,6-c net interpretation (blue and red balls, $\{5^5 \cdot 6\}_2(5^8 \cdot 6^4 \cdot 8^3)$) are given in thin yellow dashed lines. Additional structure images for **2** are given in Fig. S17 and S18, ESI†

unit contains two crystallographically independent metal ions, one deprotonated EtBCP²⁻ ligand, one DABCO ligand (the two latter represented by independent halves) and one uncoordinated DMA guest molecule (Fig. 4). The Zn1 atom has a tetrahedral environment consisting of four monoester phosphonate groups. Neighboring metal atoms are joined by the bridging monoester phosphonates, forming a linear 1D $\{Zn_2(PO_2(OEt))_2\}_n$ chain as an infinite SBU (Fig. 5a). This arrangement is relatively typical, and similar zinc and cobalt phosphonate chains are also known for instance in $[(enH_2)_2][Zn(PO_4)_2]$, $[C_{10}N_4H_{26}][Zn_5(H_2O)_4(HPO_3)_6] \cdot 4H_2O$, $[C_6N_2H_{18}][Zn_3(HPO_3)_4]$ and $[C_5N_2H_{14}][Co(HPO_4)_2]$.^{59–61} The Zn2 atom is pentacoordinated, adopting a $\{ZnO_4N\}$ square-pyramidal environment. Together with the carboxylate and DABCO ligands, the Zn2 atoms constitute the DABCO ‘capped’ $\{Zn_2(RCOO)_2(DABCO)\}_n$ paddle-wheel unit, which is also well-known.^{35,50} The DABCO associates the paddle-wheel units in a chain, so it is possible to interpret the latter as a 1D SBU, instead of the interpretation on the level of discrete paddle-wheel units.

The structure of the framework is fully determined by the geometries of the two SBUs, connected by linear organic joints (Fig. 5c). There is a clear similarity between the two 1D SBUs. Their ‘cruciform’ projections along the main axis are indistinguishable in idealized high-symmetry representation. The idealized paddle-wheel unit represents 2×2 collinear directions (D_{4h} local symmetry), which are mutually orthogonal. The idealized prototype of the $\{Zn_2(PO_2(OEt))_2\}_n$ SBU (Fig. 5a; fragment in green brackets) features the same 2×2 mutually orthogonal pairs, lying not within a single, but within two parallel planes (D_{2d} local symmetry of a translationally independent part). A very simple and efficient synergism is possible because both SBUs ensure mutually orthogonal orientations of the connecting struts.

The two types of 1D SBUs, each possessing four, pairwise orthogonal, bonding directions run parallel in the structure of **2**. The resulting framework could be interpreted to have a primitive cubic underlying net, **pcu**, if the 6-connected $\{Zn_2(PO_2(OEt))_2\}_2$ and extended paddle-wheel (*i.e.* including the DABCO-connectivity) moieties are taken as nodes

(Fig. 5a, b, d and S17, ESI†). Other interpretations are possible as infinite SBUs could be fragmented to units of finite connectivity. The interpretation above is the most ‘natural’, taking into account the geometry of the fragments and the reduction of the framework to a frequent, fundamental and easily recognizable case. Under the simplest interpretation on the level of 4-c $\{Zn_2(PO_2(OEt))_2\}$ and the 6-c paddle-wheel units the respective net is a two nodal (4-c)₂(6-c) net with a $\{5^3 \cdot 6\}_2 \{5^8 \cdot 6^4 \cdot 8^3\}$ point symbol (Fig. 5d and S17g; see ESI† for additional details).⁶²

In comparison, the structure of **1** without the bridge of still unknown origin (equivalent to DABCO regarding the connectivity) represents the well-known 4,4-c **nbo** net on the level of the 4-c $\{Zn_2(PO_2(OEt))_2\}$ and 4-c $\{Zn_2(COO)_4\}$ paddle-wheel units (Fig. S17f, ESI†).

The experimental observation of **1**, which is not reinforced by DABCO, upholds the high resilience of the structural organization of **1–3**. However, the impossibility to synthesize **1** in a large quantity and in a phase-pure form indicates that the use of DABCO is practically essential. Due to the poor quality of **1**, the nature of bridging ligands between the paddle-wheel SBU is not clear. We hypothesize that trace impurities, which also might form during the synthesis, could act as bidentate bridging ligands, analogously to DABCO. It is potentially enough to have a small amount of such molecules to produce seeds of crystals with a structural type analogous to **2**. The crystal structure of **1** suggests a site-sharing at the bridging ligand position, with a seemingly dominant contribution by solvent molecules.

The structure organization principle of **2** (Fig. 6) defines the acceptable length of the N-donor ligand with only a minor tolerance. The DABCO molecule fits nearly ideally the interstice of 6.0–7.0 Å (6.3 Å in **1** and 6.7 Å in **2**) between the paddle-wheel units. Theoretically, there is a chance also to incorporate a two-times longer ligand, like 4,4'-bipyridine (11.2 Å), when every second metal atom in the chain is absent. Such a structure is potentially possible, if every second phosphonate will not propagate the connectivity in the $\{[M_2(R'O)(R)PO_2][M_2(R''O)(R^T)PO_2]\}_n$ 1D chain-SBU. Half of the chelating ligands of the latter should be blocking monofunctional monoalkylphosphonates (with terminal substituent designated as R^T), or even monofunctional

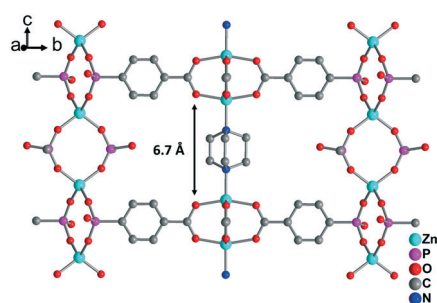


Fig. 6 A representative fragment of **2** showing the principles of structural organization. The length scaling for phosphonate ligand is potentially allowed, but not for the N-donor ligand-bridge.

carboxylate terminal co-ligands (hence, they are potentially interesting modulators). The ‘terminated’ half of the rings would not propagate connectivity, which continues for those fragments only along the 1D phosphonate chain. As a result, a **pcu** topology would ensue again, but with longer edges, compared to the underlying net of **2**.

On the other hand, the arbitrary length-scaling of the phosphonate ligand in the structure type of **2** is in principle allowed without any special conditions. The structure would scale in two out of the three directions. The retained scale along the *c*-axis should provide enough mechanical stability (MOFs with ultra-large pores, like in IRMOF-74-XI representative of the MOF-74 isorecticular series, $d_{\text{pore}} > 80$ Å, are built according to similar principles, *i.e.* geometric scaling in two out of three directions). Therefore, the structure type of **2** appears to be of general importance, as a paradigmatic instance of a potential isorecticular series.

Thermogravimetric and gas adsorption analyses

Thermogravimetric analysis (TGA) of the as-synthesized $[Zn_2(\text{EtBCP})_2(\text{DABCO})_{0.5}]\cdot 2\text{DMA}$, **2** shows a weight loss of 23.9% up to 150 °C (calc. 21.3% for two DMA molecules of the ascribed formula unit; Fig. 7a). The chemical decomposition of the compound takes place at 320 °C (Fig. 7b).

The structures of **2** and **3** feature roughly rectangular channels, running along the *c*-axis, and forming a 3D pore network *via* interconnections along other axes as well. The maximum included sphere diameter is 5.9 Å, while the maximum passable sphere diameter is 4.6 Å (as calculated by Zeo++;⁶³ here and below 3.68 Å probe diameter corresponding to N_2 is implied, if not given otherwise). The channels would be significantly larger if not the protruding ethyl groups of the ligand. However, there is a residual porosity, with a formal calculated surface area of 904–1057 $\text{m}^2 \text{g}^{-1}$. The geometrically calculated potential solvent-accessible void volume is only 4.8% for N_2 , but quickly grows to 7.3% for CO_2 (3.30 Å probe), 15.7% for H_2O (2.40 Å) and 36.7% for a formal probe of 1.0 Å diameter (Table S4†). The fast growth of the void volume is due to the narrow and curved pores, which accepts only a small amount of guest molecules with sizes approaching the pore diameter. All the

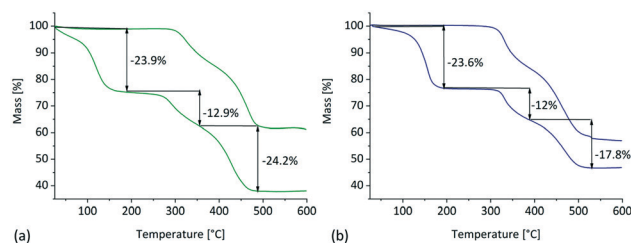


Fig. 7 TGA curves, 20–600 °C with a heating rate of 5 K min^{-1} under N_2 atmosphere for (a) the as-synthesized $[Zn_2(\text{EtBCP})_2(\text{DABCO})_{0.5}]\cdot 2\text{DMA}$, **2** (top curve) and the activated $[Zn_2(\text{EtBCP})_2(\text{DABCO})_{0.5}]\cdot 2'$ (bottom curve) (b) for the Co-analogues, **3** and **3'**.

data in this paragraph was calculated using the single crystal structure of **2** with removed solvent molecules and collapsed disorder $[\text{Zn}_2(\text{EtBCP})_2(\text{DABCO})_{0.5}]$ (Table S4, see also the comments in the ESI†).

It is important to note for the further discussion that the structural organization of **2** and **3** allows expecting enhanced flexibility due to the rotation of the phosphonate and carboxylate moieties around the axis of the 1D rod-like SBUs. Such type of flexibility is well known for carboxylate MOFs, e.g. for MIL-53, where the channels, running along the rod-like SBUs are already partially asymmetric (for example having rather a lozenge than a square shape; the latter case corresponds to a formal state of mechanic equilibrium and is much more resistant to deformation). The monoethylphosphonate differs from carboxylate by geometry (tetrahedral vs. trigonal). The $\{\text{P}(\text{OEt})\text{O}_2\text{M}_2\}$ arrangement constituting the chain SBU is out of the plane of the ligand, while the carboxylate based $\{\text{CO}_2\text{M}_2\}$, in contrary, remains coplanar, or at least co-axial, with the phenyl group after coordination. Hence, the mechanical strain, propagating along the ligand is displaced relatively to the axis of the 1D rod-like SBU and acts as a lever with ~ 2.0 Å length (for carboxylates the offset lever length is zero; the difference is very clear from Fig. 5c), which is a structural level argument for increased flexibility.

Compounds **2** and **3** were washed after the synthesis with DMA and activated at 160 °C under vacuum. The removal of the DMA guest molecules in **2** or **3** leads to a phase transition and formation of products **2'** or **3'** respectively, characterized by quite different PXRD patterns. We were not able to elucidate their structures, but the samples remain at least partially crystalline. Moreover, the soaking of **2'** or **3'** in DMA reinstates the initial structures of **2** and **3**, as witnessed by PXRD (Fig. 8 and S20, ESI†). Complete reversibility of the solvent removal is a supporting argument for retained integrity of the framework in the degassed structures, as well as for its significant flexibility.

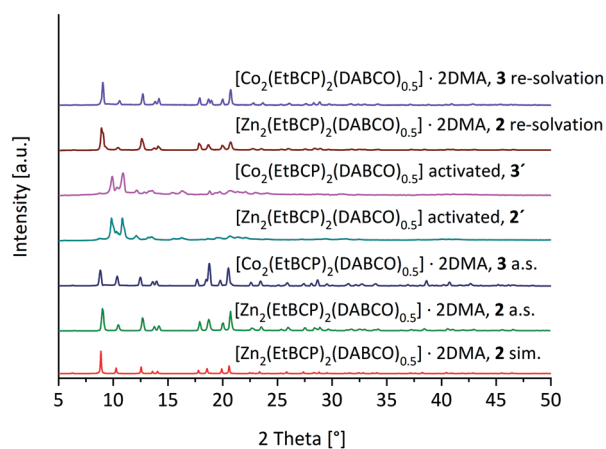


Fig. 8 Comparison of the PXRD patterns: simulated for the SCXRD structure of **2**; as-synthesized bulk **2** and **3**; activated **2'** and **3'**; re-solvated after the soaking of the activated samples in DMA.

The gas adsorption behavior of the activated $[\text{Zn}_2(\text{EtBCP})_2(\text{DABCO})_{0.5}]$, **2'**; and $[\text{Co}_2(\text{EtBCP})_2(\text{DABCO})_{0.5}]$, **3'**, materials was studied for N_2 (77 K) and Ar (87 K), CO_2 (195 K, 273 K, 293 K) and CH_4 (273 K, 293 K).

The adsorption of N_2 is negligible, which is expected for compounds with narrow pores (Fig. 9a and b). The maximum thorough sphere pore radius of 4.6 Å, assessed for the solvated structure of **2** (Table S4†), is only ~ 1 Å larger than the kinetic diameter of the N_2 molecule. The respective adsorption kinetics should be very slow, which is aggravated by a low accessible pore volume, estimated at $\sim 4.8\%$ of the total volume (Table S4†). Furthermore, even slight flexibility of the structure could decrease the pores further, rendering the compound to be non-porous. In contrary, the uptake of the kinetically slightly smaller CO_2 was significant ($115 \text{ cm}^3 \text{ g}^{-1}$ for **2'** and $128 \text{ cm}^3 \text{ g}^{-1}$ for **3'** at 1 bar, 195 K; Fig. 9), which allowed making a crude estimation of the Langmuir surface area ($P/P_0 = 0.004\text{--}0.04$ range, 195 K). The surface area of **2'** and **3'** are estimated to be $330 \text{ m}^2 \text{ g}^{-1}$ and $327 \text{ m}^2 \text{ g}^{-1}$, respectively (see ESI† for details and also for the even more imprecise BET estimation, which is, nevertheless provides comparable values).

More interestingly, the CO_2 adsorption isotherms at 195 K demonstrate two distinctive steps. The second step, starting at $P/P_0 = \sim 0.1$ could be associated with pore opening from small to larger pore size.⁶⁴ It is rather a gradual process with a relatively narrow $\sim 0.1P/P_0$ interval and could be classified as F-I type (the sudden opening, i.e. a strong rise of adsorption in a small P/P_0 is classified as F-II; the cases of **2'** and especially **3'**, with a slightly narrower interval, are approaching the latter type).⁶⁴ The Gurvich rule was used to determine the pore volume from the CO_2 adsorption isotherms at 195 K (Fig. 9a and b).⁶⁵ The micropore volume corresponding to the first step is 0.11 and $0.12 \text{ cm}^3 \text{ g}^{-1}$ for **2'** and **3'** ($P/P_0 < 0.08$ and < 0.12 respectively). The total values for the combined two steps are ~ 0.21 and $0.23 \text{ cm}^3 \text{ g}^{-1}$ (maximum estimate, $P/P_0 = 1.0$) for **2'** and **3'** respectively. Therefore, significant framework flexibility, manifesting itself in a structural transformation, was found at a low temperature (the flexible behavior was also observed for carboxylate MOFs with DABCO as a co-ligand).^{35,49,66,67}

The steep rise of the second step (tendency towards “F-II” type) suggests rather an existence of bistability than a continuity of states, which correlates well with the observed crystallinity of the as-synthesized and degassed **2** (and **3**), and yet with the strong differences of the respective PXRD patterns.

The hysteresis observed on the CO_2 adsorption isotherms for **2'** and **3'** at low pressures is kinetically conditioned. It was checked on the example of **3'** that as the equilibration time increases, the hysteresis width decreases. For the longest adsorption experiment ($\sim 5+$ times longer equilibration time per acquisition point) the adsorption and desorption branches for the first step nearly coincide, while the remaining hysteresis is nearly solely limited to the second step (see Fig. S28 and Table S5 and short corresponding

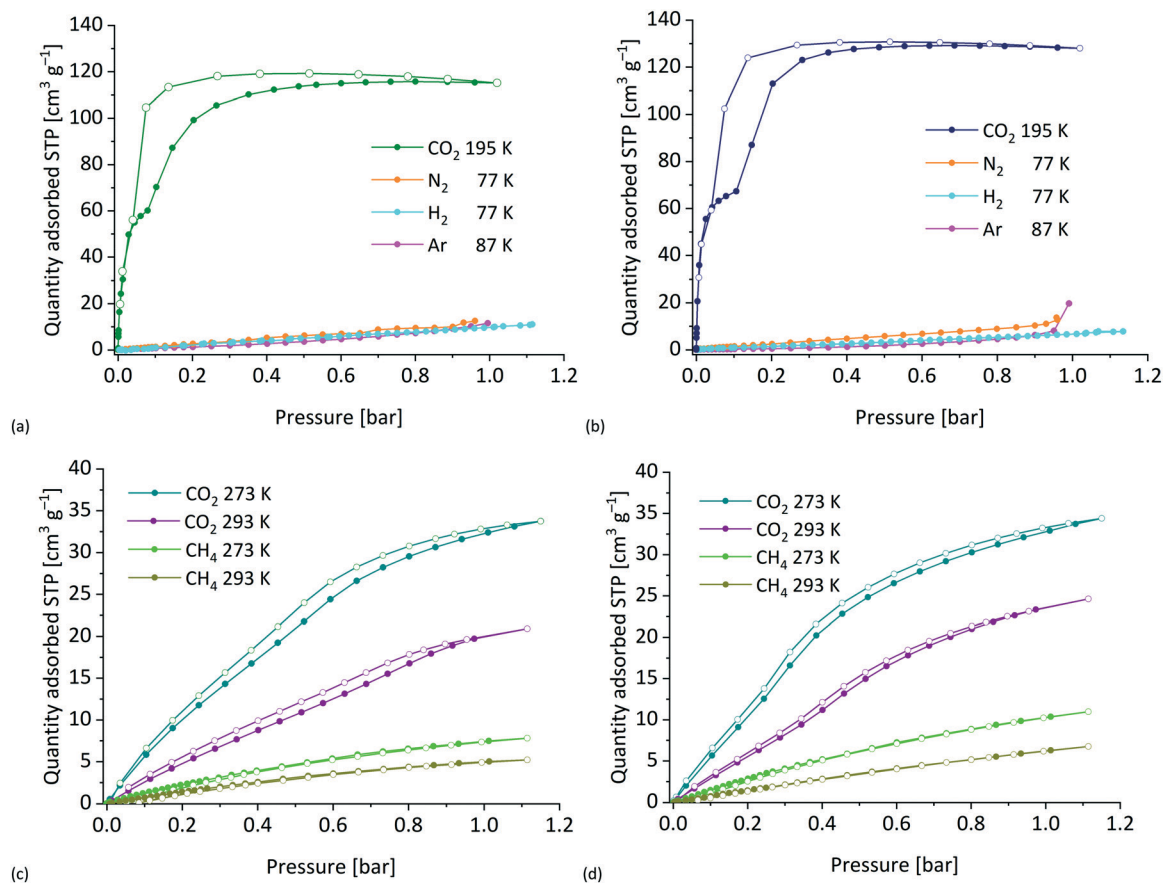


Fig. 9 Adsorption isotherms (the desorption branches are not shown for clarity in the cases of N₂, H₂ and Ar, see Fig. S23† for further details) for (a) [Zn₂(EtBCP)₂(DABCO)_{0.5}], 2'; (b) [Co₂(EtBCP)₂(DABCO)_{0.5}], 3'; (c) 2'; (d) 3'.

Table 1 CO₂ adsorption data for [Zn₂(EtBCP)₂(DABCO)_{0.5}], 2' and [Co₂(EtBCP)₂(DABCO)_{0.5}], 3' at 1 bar

Data	2'			3'		
Temperature, K	195	273	293	195	273	293
Quantity adsorbed, cm ³ g ⁻¹ (mmol g ⁻¹)	115 (5.1)	32 (1.4)	20 (0.9)	128 (5.7)	33 (1.5)	23 (1.0)

discussion in the ESI†). Hence, the desorption branch cannot be associated with a “metastable opened form”: longer equilibration times demonstrate full reversibility at least at $P/P_0 < 0.1$ pressures.

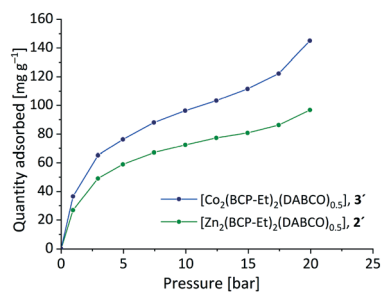


Fig. 10 High-pressure CO₂ adsorption isotherms at 298 K for 2' (green) and 3' (blue).

The heat of adsorption for CO₂ from adsorption isotherms at 273–293 K is calculated to be 33.0 and 21.0 kJ mol⁻¹ for 2' and 3' at zero coverage (Fig. S22†). The energy difference is significantly higher than expected, and we believe that the lower crystallinity of 3 should at least partially be held responsible.

The sorption data for CO₂ at 195 K, 273 K and 293 K are summarized in Table 1.

CO₂ adsorption at 298 K and 20 bar shows a larger uptake for 3' with 147 mg g⁻¹ compared to 2' with 97 mg g⁻¹ (Fig. 10). Both isotherms demonstrate inflection points at approximately 12 bar indicating possible gradual structural transformations. The dissimilarity of the transformation energetics is the only evident explanation of such a strong difference. The pore-sizes for 2', 3' are similar at low pressures at room temperature, but start to diverge at elevated pressures (note that minor, but evident

Table 2 Crystal data and refinement details for $[\text{Zn}_2(\text{EtBCP})_2(\text{DABCO})_{0.5}]-2\text{DMA}, \mathbf{2}^a$

Empirical formula	$\text{C}_{29}\text{H}_{42}\text{N}_3\text{O}_{12}\text{P}_2\text{Zn}_2$
$M/\text{g mol}^{-1}$	817.33
Crystal dimensions/mm	$0.20 \times 0.03 \times 0.03$
T/K	293
Crystal system	Tetragonal
Space group	$I4/m$
$a, b, c/\text{\AA}$	19.912 (4), 19.912 (4), 9.5338 (17)
$V/\text{\AA}^3$	3779.9 (16)
Z	4
$\rho/\text{g cm}^{-3}$	1.436
$\mu (\text{Mo K}\alpha)/\text{mm}^{-1}$	1.41
$F(000)$	1692
$T_{\text{min}}, T_{\text{max}}$	0.950, 0.958
$\Delta\rho_{\text{max}}, \Delta\rho_{\text{min}}/\text{e \AA}^{-3}$	0.81, -0.50
No. of measured, independent and observed [$I > 2\sigma(I)$] reflections	23 360, 1947, 1145
R_{int}	0.094
$R[F^2 > 2\sigma(F^2)], wR(F^2), b, S$	0.075, 0.223, 0.98

^a The CCDC reference number is 1985571. ^b $w = 1/[\sigma^2(F_o^2) + (0.1387 \times P)^2]$ where $P = (F_o^2 + 2F_c^2)/3$. Goodness-of-fit $S = [\sum[w(F_o^2 - F_c^2)^2]/(n - p)]^{1/2}$.

dissimilarities between **2'** and **3'** are visible at low pressures and low temperatures, as discussed above). The adsorption conditions (P , T) are approaching the supercritical state of CO_2 and hence the use of the Gurvich rule for the determination of the pore volume is highly questionable. Still, we have used it as an estimate: at 298 K the pore volume at the first step was calculated to be $0.11 \text{ cm}^3 \text{ g}^{-1}$ for **2'** and $0.15 \text{ cm}^3 \text{ g}^{-1}$ for **3'** (12 bar or $P/P_0 = 0.19$ in both cases) (Fig. S21, ESI†). It is presumed that after the pores are filled to a certain extent, not very different for the low (195 K) or high temperatures (298 K), a structural transformation occurs.

The notable affinity to CO_2 might partially explain another, not quite clear observation, namely the negligible adsorption of Ar, which is similar to N_2 . It is possible, that the increased adsorbent–adsorbate affinity is necessary for opening up the initially closed pores of the flexible framework.

It is interesting to compare the experimentally derived micropore volumes at the transformation points with values calculated for the structures of **2/3** (CO_2 adsorption at 195 K). The values are respectively $0.11/0.12 \text{ cm}^3 \text{ g}^{-1}$ ($P/P_0 = \sim 0.1$, 195 K), $0.11/0.15 \text{ cm}^3 \text{ g}^{-1}$ ($P/P_0 = \sim 0.19$, 195 K) **3'** vs. $0.065 \text{ cm}^3 \text{ g}^{-1}$ calculated geometrically (Table S4, ESI†). The transformations take place at an adsorption value, which corresponds reasonably well to the calculated maximum accessible pore volume for the structure of **2** with removed solvent molecules ($0.065 \text{ cm}^3 \text{ g}^{-1}$). This observation supports the viewpoint that the transformation is stimulated by complete pore filling of the less porous variant of the structure. The low precision of the estimated value should not be surprising: the calculated accessible volume in the structure of **2** quickly grows with the decrease of the size of the probe and reaches 37% for a probe of $\sim 1.0 \text{ \AA}$. While such

probe size is much smaller than a molecular size, the steep growth of the void volume shows that there is potentially available space, which could, possibly, be partially accessed upon minor structural deformations. This is what, evidently, takes place.

Moisture stability, water vapor adsorption, and liquid solvent stability tests

Both the non-degassed **2** and **3**, as well as the non-degassed **2'** and **3'** demonstrated only a minor change of PXRD patterns upon two days of exposure to ambient air (Fig. S29†). The satisfactory stability allowed to measure the water-vapour adsorption at 293 K in the range of $0-0.95P/P_0$ for the single case of **3'**, representative enough for the case of isostructural compounds. Relatively low affinity (IUPAC isotherm type III) and a maximum uptake of 48 mg g^{-1} was observed (Fig. S30†), however the very well-defined hysteresis indicates that the binding of the adsorbed water associated with the second coordination sphere of the metal ions is substantial. The relatively low affinity is in line with the hydrophobic ‘padding’ of the pores by the organic ligands and not the least by the ethyl substituent of the monoethylphosphonate, protruding into the channels. The small maximum uptake correlates well with the low accessible pore volume. The crystallinity of the sample did not change significantly during the experiment as witnessed by PXRD.

The long-term solvent exchange of **2** with chloroform, ethanol, acetone (~ 3 days each), and water (~ 1 day) was called to check the stability of the framework against liquid solvents (no prior degassing was carried out; the degassing itself is responsible for some loss of crystallinity, associated with PXRD peak broadening, which could mask finer effects, caused by the action of moisture). After PXRD measurements, the samples were exchanged again by DMA, in order to test the possibility to return to the state of crystallinity of the as-synthesized **2** (Fig. S31†). The exchange with chloroform caused minor changes, with ethanol moderate, and with acetone a transformation to another phase. However, the subsequent exchange with DMA reinstated the initial crystallinity in full, providing another argument for flexibility of the framework of **2**, this time upon the action of solvent molecules (see ESI†). On the other hand, water causes an irreversible transformation to a phase with an appreciable crystallinity, and hence **2** should be regarded as unstable to the action of liquid water for prolonged time. It is worth to stress that this instability is rather not an irreversible hydrolysis into an amorphous phase as in the majority of other MOFs, but a crystal-to-crystal transformation.

Conclusions

Two new isostructural zinc and cobalt monoethylphosphonate-carboxylate MOFs, $[\text{Zn}_2(\text{EtBCP})_2(\text{DABCO})_{0.5}]-2\text{DMA}$, **2** and $[\text{Co}_2(\text{EtBCP})_2(\text{DABCO})_{0.5}]-2\text{DMA}$, **3** including DABCO as a co-ligand were synthesized. The

structures are built upon the $\{M_2(PO_2(OEt))_2\}_n$ chains already observed in phosphonate-monoester coordination polymers and on DABCO-expanded archetypal paddle-wheel carboxylate units. A potentially very important observation for structure-design heuristics is the nearly equal length of the six-connected $\{[Zn_2(PO_2(OEt))_2]_2\}$ -phosphonate-monoester- and the $\{Zn_2(COO)_4(DABCO)\}$ SBU-fragments (in this work only the simplest, **pcu** framework is demonstrated, but due to the equivalence in dimensions a number of other framework topologies could also be expected). The structural organization shows high resilience, as the 'parent' compound, the $[Zn_2(EtBCP)_2(Bridge/Solv)] \cdot (Solv)$, **1**, was also observed as a minor product in a DABCO-free synthesis; the structural motif for **1**, similar to **2** and **3** was experimentally confirmed. Importantly, the compounds **2** and **3** represent a structural type, which permits the elongation of the monoalkylphosphonate ligand, leading to metrical scaling in two directions in isoreticular analogues (see Fig. S19†). Such scaling is preferable, comparing to the scaling in all directions, for structural stability and avoiding interpenetration. The activated compounds **2'** and **3'** show two-step CO₂ adsorption at low-pressure (195 K) and an analogous behavior with an inflection point on the isotherm at high pressure (298 K). The effects could be explained by structural flexibility, which is supported by the analysis of the structure (the 'lever' effect of the trigonal phosphonate, in contrary to trigonal-planar carboxylate, remaining in-plane with the 1D rod-like SBU as well as the particularly steep calculated growth of accessible volume in the structure by decrease of the probe size, indicating the capacities for structural rearrangement).

Experimental section

Materials and measurements

All the chemicals (purity equivalent to ACS grade or higher) were obtained from commercial sources and used without future purification.

The CHN elemental analysis was performed using Perkin Elementar Vario EL III analyzer. IR-spectra were recorded on a Bruker Tensor 37 IR spectrometer (Bruker Optics, Germany) equipped with an ATR unit. ESI-MS spectra were recorded with a Thermo-Quest Ion Trap API mass spectrometer Finnigan LCQ Deca. Thermogravimetric analysis (TGA) was performed with a Netzsch TG 209 F3 Tarsus using an aluminium crucible in the 20–600 °C range at 5 K min⁻¹ rate under N₂ atmosphere. The powder X-ray diffraction patterns (PXRDs) were obtained on a Bruker D2 Phaser diffractometer using Cu-K α radiation ($\lambda = 1.5418 \text{ \AA}$; 30 kV, 10 mA source supply parameters) and a flat low-background silicon sample holder.

The low pressure gas adsorption isotherms for CO₂, CH₄ and H₂ were measured using a Micromeritics ASAP 2020 automatic gas sorption analyzer, equipped with one vacuum pump for the sample preparation and one for the analysis ($\sim 10^{-6}$ Torr ultimate vacuum in the manifold).

The samples were degassed at the preparation port of the analyzer until the pressure rising rate in the temporarily closed manifold was less than $2 \mu\text{Torr min}^{-1}$ at 160 °C. After degassing, the sample tube was weighted (seal frits were used for permanent sealing) and transferred to the analysis port of the sorption analyzer. Before the sorption experiments, the compounds were subjected to a short, repeated degassing to remove remaining gas molecules. Helium gas was used for the determination of the warm and cold free-space of the sample tubes. The volumes of the adsorbed gases are given at standard temperature and pressure, STP (293.15 K, 101.325 kPa). The adsorption isotherms were measured for CO₂ at 195, 273, 293 K; for CH₄ at 273, 293 K and for H₂ at 77 K. The isosteric heat of adsorption values for CO₂ from the isotherms at 273.15 K and 293.0 K were calculated using Clausius–Clapeyron equation as implemented in the ASAP 2020 v3.05 software. The N₂ and Ar sorption isotherms were additionally measured on a Quantachrome Autosorb iQ MP automatic gas sorption instrument, using parameters, similar to described for the measurement with the ASAP 2020. All used gases (He, N₂, H₂, CO₂, Ar, CH₄) were of ultra-high purity (UHP, grade 5.0, 99.999%).

The CO₂ gas adsorption isotherms for 0–20 bar pressures at 298 K were measured using Rubotherm IsoSorb Static instrument, which employs a gravimetric principle. The weight change was measured with a magnetic suspension balance (resolution $0.01 \pm 0.03 \text{ mg}$).

The water vapor sorption isotherm was measured on a Quantachrome VSTAR vapor sorption analyser at 293 K.

The single crystal X-ray diffraction data were collected on a Bruker Kappa APEX II DUO equipped with an APEX II CCD area detector, using Mo-K α radiation ($\lambda = 0.71073 \text{ \AA}$) generated by a microfocus sealed tube source. The data collection was performed by ω scans and controlled by APEX2 software.⁶⁸ The data reduction was performed using SAINT⁶⁸ and the experimental absorption correction using SADABS.⁶⁹ The structure was solved by direct methods (SHELXS-2016), the refinement was done by full-matrix least squares on F^2 using the SHELXL-2018 program suite,⁷⁰ and the graphical user interface (GUI) ShelXle.⁷¹ The molecular graphics were prepared using Diamond.⁷²

Ligand synthesis

Methyl 4-iodobenzoate. The procedure was adapted from Zhao *et al.*⁷³ Concentrated H₂SO₄ (5 mL) was carefully added to a solution of 4-iodobenzoic acid (10 g, 0.04 mol) in MeOH (200 mL). The mixture was refluxed for 14 h. After cooling to room temperature, the solvent was removed *in vacuo* and the residue was dissolved in dichloromethane (100 mL). The organic layer was washed with saturated NaHCO₃ solution (100 mL), brine (100 mL) and dried over MgSO₄. Methyl 4-iodobenzoate was obtained as a white solid after removal of the solvent under reduced pressure (9.6 g, 91%); ¹H NMR (300 MHz, CDCl₃): δ 7.80 (d, $J = 8.6 \text{ Hz}$, 2H), 7.73 (d, $J = 8.6$

Hz, 2H), 3.91 (s, 3H); ^{13}C NMR (75 MHz, CDCl_3): δ = 166.7, 137.9, 131.2, 129.7, 100.9, 52.4.

Methyl 4-(diethoxyphosphoryl)benzoate. The procedure was adapted from Jaffrès *et al.*⁷⁴ A stirred mixture of NiBr_2 (0.87 g; 4 mmol), methyl 4-iodobenzoate (13.0 g, 50 mmol) and mesitylene (14 mL) were heated to 180 °C under nitrogen atmosphere. Triethylphosphite (12.8 mL, 75 mmol) was added dropwise for 4 h. During the addition of triethylphosphite, a color change of the solution from red to violet and finally to yellow was observed. After the addition, the solution was heated further at 180 °C for 2 h yielding a yellow suspension. Then, the solvent was removed *in vacuo*. Water (100 mL) was added to the residue and the mixture extracted with diethyl ether (2 × 50 mL). The organic phase was washed with brine (50 mL) and dried over MgSO_4 . The reaction mixture was concentrated *in vacuo* to produce an orange viscous oil that was purified by silica gel column chromatography using (DCM/EtOH: 98/2) as eluent to give a colorless viscous oil of methyl 4-(diethoxyphosphoryl)benzoate (7.1 g, 52%); ^{31}P NMR (121 MHz, CDCl_3): δ = 17.68; ^1H NMR (300 MHz, $\text{DMSO}-d_6$): δ 8.09 (dd, $^3J = 8.5$, $^4J = 3.8$ Hz, 2H), 7.86 (dd, $^3J = 12.8$, $^3J = 8.5$ Hz, 2H), 4.14–3.97 (m, 4H), 3.88 (s, 3H), 1.23 (t, $J = 7.2$ Hz, 6H); ^{13}C NMR (75 MHz, $\text{DMSO}-d_6$) δ 165.5, 133.4, 132.9, 131.7, 129.2, 62.0, 52.5.

O-Ethyl-P-(4-carboxyphenyl)phosphonic acid or 4-(ethoxyhydroxyphosphinyl)benzoic acid (H_2EtBCP). The procedure is adapted from Lee *et al.*⁴⁵ Methyl-4-(diethoxyphosphoryl)benzoate (1.5 g, 5.5 mmol) was heated in a mixture of aqueous NaOH (2 mol L^{-1} , 33 mL) and EtOH (33 mL) at 80 °C during 3 h. The reaction mixture was then concentrated *in vacuo* to a third of the volume and acidified with cooled 1 N HCl to pH 1, followed by extraction with dichloromethane. The combined organic extracts were dried over Na_2SO_4 and the solvent was removed under reduced pressure, to afford the product as a white solid (0.71 g, 56%); ^{31}P NMR (121 MHz, $\text{DMSO}-d_6$): δ = 14.61; ^1H NMR (300 MHz, $\text{DMSO}-d_6$) δ 8.04 (dd, $J = 8.4$, $J = 3.6$ Hz, 2H), 7.81 (dd, $J = 12.6$, $J = 8.4$ Hz, 2H), 3.96–3.86 (m, 2H), 1.18 (t, $J = 7.1$ Hz, 3H); ^{13}C NMR (75 MHz, $\text{DMSO}-d_6$) δ 166.79, 135.9, 133.5, 131.3, 129.2, 61.0, 16.3.

MOF syntheses

Synthesis of $[\text{Zn}_2(\text{EtBCP})_2(\text{DABCO})_{0.5}]\cdot 2\text{DMA}$, 2; $[\text{Co}_2(\text{EtBCP})_2(\text{DABCO})_{0.5}]\cdot 2\text{DMA}$, 3. The compounds 2 and 3 were synthesized according to the same procedure (for the synthesis of $[\text{Zn}_2(\text{EtBCP})_2(\text{Solv})]\cdot \text{Solv}'$, 1, see ESI†). $\text{Zn}_2(\text{NO}_3)_2\cdot 6\text{H}_2\text{O}$ (26.77 mg, 0.09 mmol) or $\text{Co}_2(\text{NO}_3)_2\cdot 6\text{H}_2\text{O}$ (26.2 mg, 0.09 mmol), DABCO (5 mg, 0.045 mmol) and H_2EtBCP (20 mg, 0.09 mmol) were dissolved in DMA (2 mL). The mixture was transferred in a thick-walled borosilicate glass tube, sealed with a screw-cap and heated up to 100 °C for 8 h. The temperature was held for 94 h and then decreased linearly to room temperature within 4 h. 34.6 mg (60%) of 2 consisting of considerably large colorless single crystals and 37.2 mg (66%) of 3 consisting of very small dark-blue single crystals,

too small for a routine SCXRD experiment, were collected. The syntheses were reproduced six times.

2 Elemental analysis [%] calc. for: $[\text{Zn}_2(\text{EtBCP})_2(\text{DABCO})_{0.5}]\cdot 2\text{DMA}$, $\text{C}_{29}\text{H}_{42}\text{N}_3\text{O}_{12}\text{P}_2\text{Zn}_2$: C 42.61, H 5.18, N 5.14, found: C 42.3, H 5.17, N 5.01. IR (KBr) $\tilde{\nu}_{\text{max}}$ [cm^{-1}]: 3440, 2982, 2937, 1644, 1556, 1414, 1190, 1156, 1129, 1090, 1046, 1014, 965, 868, 848, 807, 776, 732, 703, 520, 484.

2' (degassed 2). Elemental analysis [%] calc. for: $[\text{Zn}_2(\text{EtBCP})_2(\text{DABCO})_{0.5}]$, $\text{C}_{21}\text{H}_{24}\text{NO}_{10}\text{P}_2\text{Zn}_2$: C 39.22, H 3.76, N 2.18, found: C 38.48, H 3.68, N 2.14. IR (KBr) $\tilde{\nu}_{\text{max}}$ [cm^{-1}]: 3436, 3068, 2981, 2934, 2902, 1636, 1553, 1503, 1419, 1157, 1128, 1079, 1042, 948, 863, 771, 729, 702, 608, 476.

3 Elemental analysis [%] calc. for: $[\text{Co}_2(\text{EtBCP})_2(\text{DABCO})_{0.5}]\cdot 2\text{DMA}$, $\text{C}_{29}\text{H}_{42}\text{N}_3\text{O}_{12}\text{P}_2\text{Co}_2$: C 43.30, H 5.26, N 5.22, found: C 43.07, H 2.27, N 5.11. IR (KBr) $\tilde{\nu}_{\text{max}}$ [cm^{-1}]: 3435, 2981, 2936, 2902, 1649, 1553, 1450, 1413, 1264, 1189, 1155, 1129, 1088, 1046, 1014, 867, 846, 806, 505, 775, 732, 703, 591, 491.

3' EA [%] calc. for: $[\text{Co}_2(\text{EtBCP})_2(\text{DABCO})_{0.5}]$, $\text{C}_{21}\text{H}_{24}\text{NO}_{10}\text{P}_2\text{Co}_2$: C 40.02, H 3.84, N 2.22, found: C 39.28, H 3.91, N 2.15. IR (KBr) $\tilde{\nu}_{\text{max}}$ [cm^{-1}]: 3433, 3065, 2980, 2935, 2900, 1620, 1551, 1503, 1413, 1287, 1157, 1128, 1076, 1043, 948, 863, 771, 729, 704, 608, 482.

Structure refinement details

The DABCO molecule is located on the 4-fold axis special position. The trigonal molecule has a lower symmetry than the symmetry of the special position. The disorder was modeled using a four-component model with equal weights. The ethyl group of the ligand was refined using a two-component disorder model with equally populated components related by a mirror plane. The disordered DMA molecule was modeled similarly. All atoms in the structure except the DMA guest molecule were refined anisotropically. A part of the C–O, C–N, C–C, and N–O bond lengths in the OEt moiety and the guest solvent molecule were restrained. The hydrogen atoms of DABCO, DMA and the ethyl group of the ligand were positioned geometrically and refined using a riding model: $d(\text{C–H}) = 0.96 \text{ \AA}$ (CH_2), 0.97 \AA (CH_3), 0.95 \AA ($\text{C}_{\text{Ar}}\text{H}$); $U_{\text{iso}}(\text{H}) = 1.2 \times U_{\text{eq}}$. The crystal data and structure refinement details are given in Table 2.

Conflicts of interest

There are no conflicts to declare.

Acknowledgements

The authors thank one of our anonymous referee, who posed interesting questions regarding the role of the *in situ* formed formic acid, as well as the hysteresis and kinetic effects for the CO_2 adsorption, which allowed to improve the manuscript. We thank Dr. Gamall Makhouloufi, then a doctoral student in the group of CJ, for collecting preliminary data for the “predecessor” structure of 1.

References

- 1 W. Lu, Z. Wei, Z. Y. Gu, T. F. Liu, J. Park, J. Park, J. Tian, M. Zhang, Q. Zhang, T. Gentle III, M. Bosch and H. C. Zhou, *Chem. Soc. Rev.*, 2014, **43**, 5561–5593.
- 2 G. K. Shimizu, R. Vaidhyanathan and J. M. Taylor, *Chem. Soc. Rev.*, 2009, **38**, 1430–1449.
- 3 J. P. Zhang, Y. B. Zhang, J. B. Lin and X. M. Chen, *Chem. Rev.*, 2012, **112**, 1001–1033.
- 4 M. F. de Lange, K. J. Verouden, T. J. Vlugt, J. Gascon and F. Kapteijn, *Chem. Rev.*, 2015, **115**, 12205–12250.
- 5 Y. B. Huang, J. Liang, X. S. Wang and R. Cao, *Chem. Soc. Rev.*, 2017, **46**, 126–157.
- 6 J.-R. Li, R. J. Kuppler and H.-C. Zhou, *Chem. Soc. Rev.*, 2009, **38**, 1477–1504.
- 7 L. E. Kreno, K. Leong, O. K. Farha, M. Allendorf, R. P. Van Duyne and J. T. Hupp, *Chem. Rev.*, 2012, **112**, 1105–1125.
- 8 J. Hynek, P. Brázda, J. Rohlíček, M. G. S. Londesborough and J. Demel, *Angew. Chem., Int. Ed.*, 2018, **57**, 5016–5019.
- 9 P. Deria, W. Bury, I. Hod, C. W. Kung, O. Karagiari, J. T. Hupp and O. K. Farha, *Inorg. Chem.*, 2015, **54**, 2185–2192.
- 10 Y.-P. Zhu, T.-Y. Ma, Y.-L. Liu, T.-Z. Ren and Z.-Y. Yuan, *Inorg. Chem. Front.*, 2014, **1**, 360–383.
- 11 S. R. Miller, G. M. Pearce, P. A. Wright, F. Bonino, S. Chavan, S. Bordiga, I. Margiolaki, N. Guillou, G. Férey, S. Bourrelly and P. L. Llewellyn, *J. Am. Chem. Soc.*, 2008, **130**, 15967–15981.
- 12 M. T. Wharmby, J. P. Mowat, S. P. Thompson and P. A. Wright, *J. Am. Chem. Soc.*, 2011, **133**, 1266–1269.
- 13 Y. Zorlu, D. Erbahar, A. Cetinkaya, A. Bulut, T. S. Erkal, A. O. Yazaydin, J. Beckmann and G. Yucesan, *Chem. Commun.*, 2019, **55**, 3053–3056.
- 14 N. Hermer and N. Stock, *Dalton Trans.*, 2015, **44**, 3720–3723.
- 15 T. Zheng, Z. Yang, D. Gui, Z. Liu, X. Wang, X. Dai, S. Liu, L. Zhang, Y. Gao, L. Chen, D. Sheng, Y. Wang, J. Diwu, J. Wang, R. Zhou, Z. Chai, T. E. Albrecht-Schmitt and S. Wang, *Nat. Commun.*, 2017, **8**, 15369–15379.
- 16 Z. Hassanzadeh Fard, N. E. Wong, C. D. Malliakas, P. Ramaswamy, J. M. Taylor, K. Otsubo and G. K. H. Shimizu, *Chem. Mater.*, 2018, **30**, 314–318.
- 17 Z. H. Fard, Y. Kalinovsky, D. M. Spasyuk, B. A. Blight and G. K. H. Shimizu, *Chem. Commun.*, 2016, **52**, 12865–12868.
- 18 T. Zeng, L. Wang, L. Feng, H. Xu, Q. Cheng and Z. Pan, *Dalton Trans.*, 2019, **48**, 523–534.
- 19 L.-L. Dai, Y.-Y. Zhu, C.-Q. Jiao, Z.-G. Sun, S.-P. Shi, W. Zhou, W.-Z. Li, T. Sun, H. Luo and M. X. Ma, *CrystEngComm*, 2014, **16**, 5050–5061.
- 20 D. Kong, J. Zon, J. McBee and A. Clearfield, *Inorg. Chem.*, 2006, **45**, 977–986.
- 21 Z. Zhao, D. Yang, B. Xing, C. Ma, Z.-G. Sun, Y.-Y. Zhu, H.-Y. Li and J. Li, *RSC Adv.*, 2016, **6**, 92175–92185.
- 22 C. Ma, C.-Q. Jiao, Z.-G. Sun, Y.-Y. Zhu, X.-W. Zhang, M. L. Wang, D. Yang, Z. Zhao, H.-Y. Li and B. Xing, *RSC Adv.*, 2015, **5**, 79041–79049.
- 23 Z. Chen, H. Yang, M. Deng, Y. Ling, L. Weng and Y. Zhou, *Dalton Trans.*, 2012, **41**, 4079–4083.
- 24 S.-P. Shi, Y.-Y. Zhu, Z.-G. Sun, W. Zhou, L.-L. Dai, M.-X. Ma, W.-Z. Li, H. Luo and T. Sun, *Cryst. Growth Des.*, 2014, **14**, 1580–1590.
- 25 K. Chen, Z.-G. Sun, Y.-Y. Zhu, Z.-M. Liu, F. Tong, D.-P. Dong, J. Li, C.-Q. Jiao, C. Li and C.-L. Wang, *Cryst. Growth Des.*, 2011, **11**, 4623–4631.
- 26 T.-H. Zhou, Z.-Z. He, X. Xu, X.-Y. Qian and J.-G. Mao, *Cryst. Growth Des.*, 2013, **13**, 838–843.
- 27 A. M. Putz, L. M. Carrella and E. Rentschler, *Dalton Trans.*, 2013, **42**, 16194–16199.
- 28 J.-T. Li, T. D. Keene, D.-K. Cao, S. Decurtins and L.-M. Zheng, *CrystEngComm*, 2009, **11**, 1255–1260.
- 29 X. Chen, Y. Peng, X. Han, Y. Liu, X. Lin and Y. Cui, *Nat. Commun.*, 2017, **8**, 2171.
- 30 Y.-J. Qi, J.-H. Liu, W.-X. Zheng, X.-X. Li and S.-T. Zheng, *Chin. Chem. Lett.*, 2018, 959–962.
- 31 C. Serre, N. Stock, T. Bein and G. Férey, *Inorg. Chem.*, 2004, **43**, 3159–3163.
- 32 C. Heering, B. Francis, B. Nateghi, G. Makhoulfi, S. Lüdeke and C. Janiak, *CrystEngComm*, 2016, **18**, 5209–5223.
- 33 C. Zhang, H. Shi, L. Sun, Y. Yan, B. Wang, Z. Liang, L. Wang and J. Li, *Cryst. Growth Des.*, 2018, **18**, 7683–7689.
- 34 K. Seki and W. Mori, *J. Phys. Chem. B*, 2002, **106**, 1380–1385.
- 35 D. N. Dybtsev, H. Chun and K. Kim, *Angew. Chem., Int. Ed.*, 2004, **43**, 5033–5036.
- 36 S. S. Iremonger, J. Liang, R. Vaidhyanathan, I. Martens, G. K. H. Shimizu, T. D. Daff, M. Z. Aghaji, S. Yeganegi and T. K. Woo, *J. Am. Chem. Soc.*, 2011, **133**, 20048–20051.
- 37 K. Bladek, M. Reid, H. Nishihara, F. Akhtar, B. Gelfand and G. K. H. Shimizu, *Chem. – Eur. J.*, 2018, **24**, 1533–1538.
- 38 B. Gelfand, J. Taylor and G. K. H. Shimizu, *CrystEngComm*, 2017, **19**, 3727–3736.
- 39 B. S. Gelfand, R. P. Huynh, R. K. Mah and G. K. H. Shimizu, *Angew. Chem., Int. Ed.*, 2016, **55**, 14614–14617.
- 40 B. Gelfand, J.-B. Lin and G. K. H. Shimizu, *Inorg. Chem.*, 2015, **54**, 1185–1187.
- 41 B. Gelfand, R. P. S. Huynh, S. Collins, T. Woo and G. K. H. Shimizu, *Chem. Mater.*, 2017, **29**, 10469–10477.
- 42 S. S. Iremonger, J. Liang, R. Vaidhyanathan and G. K. H. Shimizu, *Chem. Commun.*, 2011, **47**, 4430–4432.
- 43 J. M. Taylor, R. Vaidhyanathan, S. S. Iremonger and G. K. H. Shimizu, *J. Am. Chem. Soc.*, 2012, **134**, 14338–14340.
- 44 J.-W. Zhang, C.-C. Zhao, Y.-P. Zhao, H.-Q. Xu, Z.-Y. Du and H.-L. Jiang, *CrystEngComm*, 2014, **16**, 6635–6644.
- 45 Y. Park, I. Jeon, S. Shin, J. Min and P. H. Lee, *J. Org. Chem.*, 2013, **78**, 10209–10220.
- 46 Y. Park, J. Seo, S. Park, E. J. Yoo and P. H. Lee, *Chem. – Eur. J.*, 2013, **19**, 16461–16468.
- 47 R. W. Heidebrecht, M. Chenard, J. Close, W. K. Dahlberg, J. Fleming, J. B. Grimm, J. E. Hamill, A. Harsch, B. B. Haines, B. Hughes, A. M. Kral, R. E. Middleton, C. Mushti, N. Ozerova, A. A. Szweczak, H. Wang, K. Wilson, D. J. Witter, J. P. Secrist and T. A. Miller, *Bioorg. Med. Chem. Lett.*, 2009, **19**, 2053–2058.
- 48 T. N. Tu, K. D. Nguyen, T. N. Nguyen, T. Truong and N. T. S. Phan, *Catal. Sci. Technol.*, 2016, **6**, 1384–1392.

- 49 S. Henke, A. Schneemann, A. Wütscher and R. A. Fischer, *J. Am. Chem. Soc.*, 2012, **134**, 9464–9474.
- 50 H. Wang, J. Getzschmann, I. Senkovska and S. Kaskel, *Microporous Mesoporous Mater.*, 2008, **116**, 653–657.
- 51 B. Chen, S. Ma, F. Zapata, F. R. Fronczek, E. B. Lobkovsky and H. C. Zhou, *Inorg. Chem.*, 2007, **46**, 1233–1236.
- 52 B.-Q. Ma, K. L. Mulfort and J. T. Hupp, *Inorg. Chem.*, 2005, **44**, 4912–4914.
- 53 S. Bureekaew, H. Sato, R. Matsuda, Y. Kubota, R. Hirose, J. Kim, K. Kato, M. Takata and S. Kitagawa, *Angew. Chem., Int. Ed.*, 2010, **49**, 7660–7664.
- 54 H. Chun, D. N. Dybtsev, H. Kim and K. Kim, *Chem. – Eur. J.*, 2005, **11**, 3521–3529.
- 55 V. Guillermin, D. Kim, J. F. Eubank, R. Luebke, X. Liu, K. Adil, M. S. Lah and M. Eddaoudi, *Chem. Soc. Rev.*, 2014, **43**, 6141–6172.
- 56 K. Uemura, Y. Yamasaki, Y. Komagawa, K. Tanaka and H. Kita, *Angew. Chem., Int. Ed.*, 2007, **46**, 6662–6665.
- 57 S. Takamizawa, T. Akatsuka and R. Miyake, *CrystEngComm*, 2010, **12**, 82–84.
- 58 M. Kondo, Y. Takashima, J. Seo, S. Kitagawa and S. Furukawa, *CrystEngComm*, 2010, **12**, 2350–2353.
- 59 K. Yanxiong, L. Jianmin, Z. Yugen, H. Gaofei, J. Zheng and L. Zhibin, *Cryst. Res. Technol.*, 2002, **37**, 169–175.
- 60 W. Fu, D. Zhang, Z. Shi, L. Yang and S. Feng, *Inorg. Chim. Acta*, 2006, **359**, 369–373.
- 61 A. Choudhury, S. Natarajan and C. N. R. Rao, *J. Chem. Soc., Dalton Trans.*, 2000, 2595–2598.
- 62 V. A. Blatov, A. P. Shevchenko and D. M. Proserpio, *Cryst. Growth Des.*, 2014, **14**, 3576–3586.
- 63 T. F. Willems, C. H. Rycroft, M. Kazi, J. C. Meza and M. Haranczyk, *Microporous Mesoporous Mater.*, 2012, **149**, 134–141.
- 64 Q.-Y. Yang, P. Lama, S. Sen, M. Lusi, K. J. Chen, W.-Y. Gao, M. Shivanna, T. Pham, N. Hosono, S. Kusaka, J. J. Perry IV, S. Ma, B. Space, L. J. Barbour, S. Kitagawa and M. J. Zaworotko, *Angew. Chem., Int. Ed.*, 2018, **57**, 5684–5689.
- 65 L. Gurvich, *Zh. Russ. Fiz.-Khim. O-va.*, 1915, **47**, 805–827.
- 66 A. Schneemann, P. Vervoorts, I. Hante, M. Tu, S. Wannapaiboon, C. Sternemann, M. Paulus, D. C. F. Wieland, S. Henke and R. A. Fischer, *Chem. Mater.*, 2018, **30**, 1667–1676.
- 67 K. Uemura, Y. Yamasaki, Y. Komagawa, K. Tanaka and H. Kita, *Angew. Chem.*, 2007, **119**, 6782–6785.
- 68 Bruker AXS, *APEX2*, Bruker AXS Inc., Madison, Wisconsin, USA, 2012.
- 69 G. M. Sheldrick, *In Program SADABS: Area-detector absorption correction*, University of Göttingen, Germany, 1996.
- 70 G. M. Sheldrick, Crystal structure refinement with SHELXL, *Acta Crystallogr., Sect. C: Struct. Chem.*, 2015, **71**, 3–8.
- 71 C. B. Hübschle, G. M. Sheldrick and B. Dittrich, ShelXle: a Qt graphical user interface for SHELXL, *J. Appl. Crystallogr.*, 2011, **44**, 1281–1284.
- 72 K. Brandenburg, *Diamond (Version 3.2), Crystal and Molecular Structure Visualization, Crystal Impact*, K. Brandenburg & H. Putz Gbr, Bonn (Germany), 2009, <http://www.crystalimpact.com/diamond>.
- 73 M. Shao and Y. Zhao, *Tetrahedron Lett.*, 2010, **51**, 2892–2895.
- 74 J.-M. Rueff, N. Barrier, S. Boudin, V. Dorcet, V. Caignaert, P. Boullay, G. Hix and P.-A. Jaffrès, *Dalton Trans.*, 2009, 10614–10620.